

SCIENTIFIC REPORTS



OPEN

Imaging and mechanical characterization of different junctions in spider orb webs

Gabriele Greco^{1,2}, Maria F. Pantano¹, Barbara Mazzolai² & Nicola M. Pugno^{1,3,4}

Spider silk and spider orb webs are among the most studied biological materials and structures owing to their outstanding mechanical properties. A key feature that contributes significantly to the robustness and capability to absorb high kinetic energy of spider webs is the presence of junctions connecting different silk threads. Surprisingly, in spite of their fundamental function, the mechanics of spider web junctions have never been reported. Herein, through mechanical characterization and imaging, we show for the first time that spider orb webs host two different types of junction, produced by different silk glands, which have different morphology, and load bearing capability. These differences can be explained in view of the different roles they play in the web, i.e. allowing for a localized damage control or anchoring the whole structure to the surrounding environment.

Spider silk is a unique protein-based material produced by the silk glands of spiders^{1–3}. Owing to its outstanding mechanical properties, which have been investigated in depth^{4–8}, spider silk is currently under consideration for different applications, ranging from engineering to medicine^{9–13}. During their evolution, spiders have used their silk for a variety of purposes, including production of egg sacs, mating behavior, self-defense and prey capture^{1,2,14}. For the capture of prey, the orb-web (Fig. 1a) is one of the most effective structures developed by nature¹⁵.

From a mechanical point of view, the behavior of the orb-web under external loads due to wind and impacts has been studied mainly through a numerical approach^{16,17}. It was found that the spider's web can resist extreme wind conditions owing to the presence of specific anchorages that securely fix it to a surface¹⁸. From a structural point of view, these anchorages, or attachment discs, consist of very thin (~tens of nanometers in diameter) fibers embedded in a matrix with an unknown chemical composition^{19–21} (Fig. 1b). The mechanical properties of such discs were intensively investigated through both theoretical and experimental studies. In particular, their mechanical behavior was studied through the theory of multiple peeling and its numerical implementation^{22,23}. More recently, experiments were performed in order to derive the peeling force required to detach spider silk anchorages from different substrates (Fig. 1b–d)^{24–26}.

Besides anchorages, other important features contribute significantly to the performances of the spider's web. These are the junctions connecting different threads to one another (Fig. 1e)²⁷ within the same web (Fig. 1a). At junctions, web threads interact in a synergistic fashion that provides the whole structure with its unique capability of minimizing the area damaged by the impact of an object, e.g. flies¹⁷. However, despite their fundamental role, spider web junctions have never been deeply characterized. Thus, herein we focus specifically on the role played by these structural elements and we give special attention to their morphology and mechanical properties.

In the literature, it is commonly accepted that junctions result from localized deposition of a silk-secretion produced by the piriform glands of spiders², which are the same glands that produce the silk used for the attachment discs (Fig. 1b,e). However, the experimental evidence of this work, in agreement with Vasanthavada *et al.*²⁸, shows that aggregate glands, which are normally used to produce the glue droplets in the catching spiral threads²⁹ (Fig. 2a,b), are involved, too.

Finally, in order to explain the need for the presence of two different junctions in the orb web, we performed, for the first time, both morphological analyses and mechanical characterization tests.

¹Laboratory of Bio-Inspired & Graphene Nanomechanics, Department of Civil, Environmental and Mechanical Engineering, University of Trento, Via Mesiano, 77, 38123, Trento, Italy. ²Center for Micro-BioRobotics@SSSA, Istituto Italiano di Tecnologia, Viale Rinaldo Piaggio 34, I-56025, Pontedera, Italy. ³School of Engineering and Materials Science, Queen Mary University of London, Mile End Road, E1 4NS, London, United Kingdom. ⁴Ket-Lab, Edoardo Amaldi Foundation, Via del Politecnico snc, 00133, Rome, Italy. Correspondence and requests for materials should be addressed to N.M.P. (email: nicola.pugno@unitn.it)

Received: 7 June 2018

Accepted: 5 March 2019

Published online: 08 April 2019

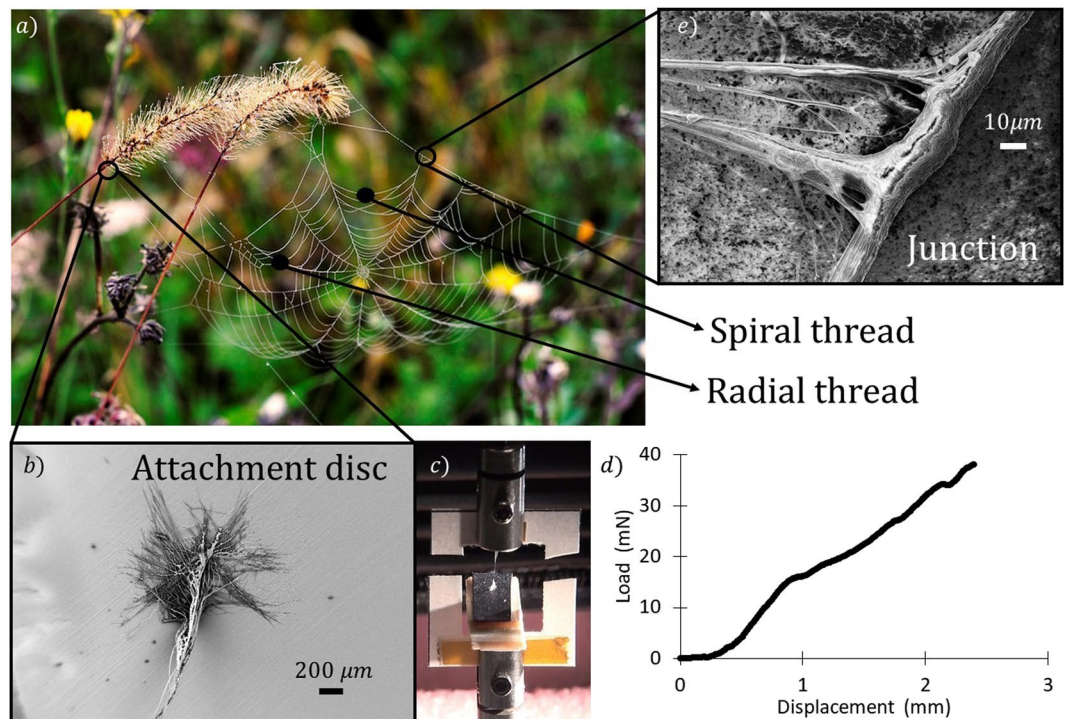


Figure 1. (a) Picture of an orb-web structure (courtesy of Federica Fabietti), including radial and spiral threads, as indicated by the arrows. Adjacent threads are held together at junction points. The whole web structure is fixed to the ground by attachment discs. (b) SEM picture of an attachment disc, produced by *Nuctenea umbratica* that anchors the web to a substrate. (c) A web anchorage under mechanical characterization through a nanotensile testing machine. Here a dangling silk fiber connected to the disc is pulled until the disc is completely detached from its paper substrate, providing the load-displacement curve reported in (d). (e) SEM picture of a junction connecting a spiral and a radial thread isolated from an orb web produced by the species *Nuctenea umbratica*; the junction was not metalized.

Results

In the web structure we can identify two kinds of junction according to the type of the involved threads (either spiral or radial, Fig. 2b,c). If we compare their morphology (Fig. 2d,e and 3), several differences emerge. Junctions between radial threads, which are those occurring along the edges of the web (Fig. 2e) or where this is fixed to the substrate, have a multiple fibril shape. This morphology is similar to that of the attachment disc (Fig. 1b) and could be thus produced by the piriform glands as well². On the other hand, junctions that involve both radial and spiral threads look completely different (Fig. 2d). Indeed, they consist of a glue drop that looks like the droplets in catching spiral threads (Figs 2b and 3a–c). Thus, similarly to these latter, they could be produced by aggregate glands, too. The role of the aggregate glands in the production of this kind of junctions in orb web has never been reported, but only observed in 3D cob web by Vasanthavada *et al.*²⁸.

In order to evaluate the mechanical properties of all the orb web junctions, we isolated from the orb web five different samples, each involving a specific number of junctions and silk threads (Fig. 3): (a) T-shaped spiral-to-radial junction (TSR), (b) Cross-shaped spiral-radial junction (CSR), (c) Net-shaped spiral-to-radial junction (NSR), (d) T-shaped radial-to-radial junction (TRR), and radial-from-surface junction (RFS, here reported for the sake of comparison with the literature). The first tested configuration (a) consists of a spiral thread joined nearly perpendicular to a radial thread by aggregate silk glue (Fig. 3a). The second (b) is similar to the previous one, but with another spiral thread that is arranged normal to the radial thread, thus resulting in a cross shape with aggregate glue at the middle (Fig. 3b). The third tested configuration (c) belongs to a more complex web structure, composed of a supporting radial thread that crosses four perpendicular spiral threads that are connected through aggregate silk (Fig. 3c). The fourth tested configuration (d) has a T shape that differs from type (a), as it consists of only radial threads joined together by a multifibril structure that recalls the piriform silk morphology (Fig. 3d). The fifth sample (Fig. 1b–d) is the whole attachment disc of the web as produced by the piriform gland.

In order to investigate the mechanical properties, ten replications for each junction typology were considered, where either a spiral or radial thread was pulled out of its junction (Figs 2f–h, S1–S6, Tables S1–S5 and Videos S1–S5). We found that the mean force necessary to break TSR junctions (type a) was 0.4 ± 0.2 mN, with dissipated energy of 1.5 ± 1.1 μJ and mean displacement at break of 9 ± 4 mm (Fig. 4). We noticed that after failure the supporting radial thread remained undamaged (Fig. S2). For the CSR junction (type b), we found that the mean force at break was 0.9 ± 0.2 mN, its dissipated energy was 3.4 ± 1.8 μJ and its mean displacement at break was 10 ± 5 mm (Fig. 4). The supporting structure resulted unbroken after the break of the junction also in this

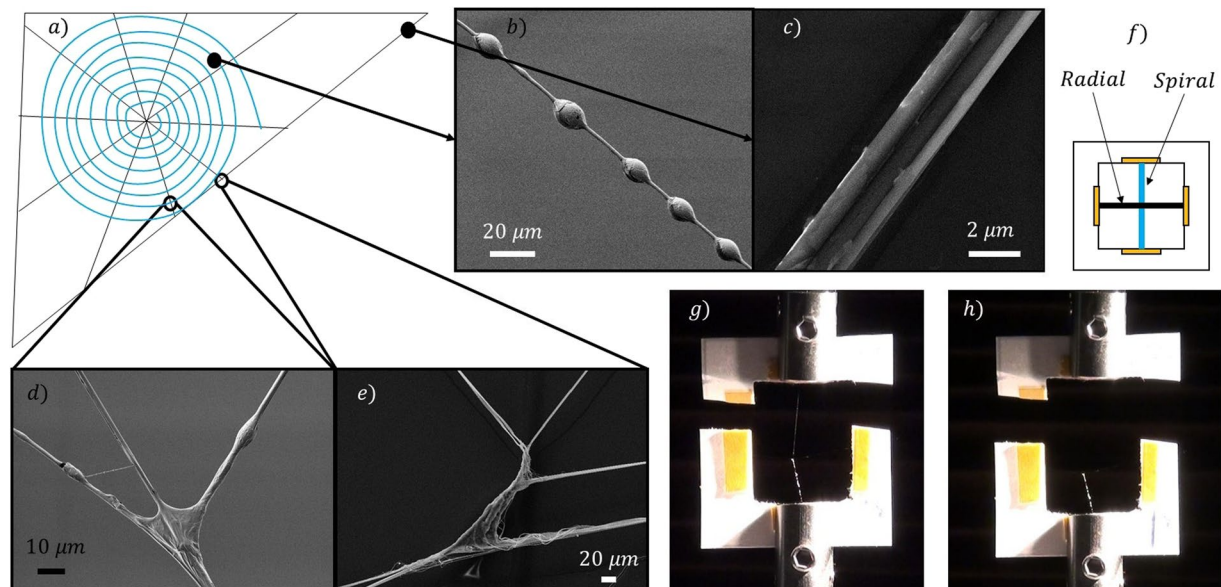


Figure 2. (a) Schematic of an orb web, consisting of spiral (b) and radial (c) threads. (d) SEM picture of a junction involving two spiral threads and one radial thread. (e) SEM picture of a junction between two radial threads. Significant difference can be observed between the two types of junction. (f) Schematic of a web sample mounted on a paper frame to test junction structural properties. (g) Junction sample under mechanical characterization through a nanotensile testing machine and (h) the remaining structure after junction failure.

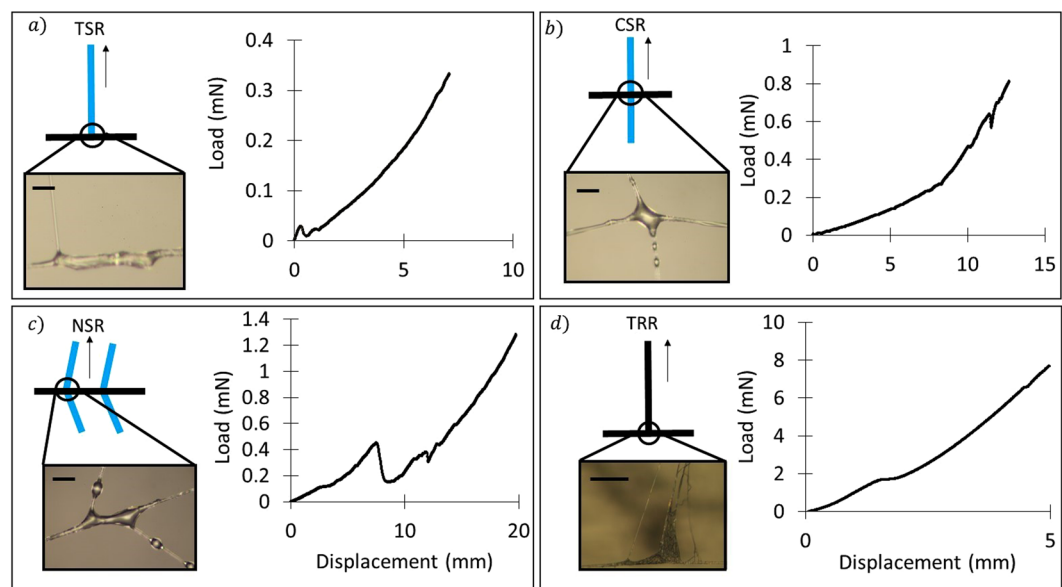


Figure 3. Example Load/Displacement curves derived from testing different web samples, each involving a different number/type of silk threads and junctions. These curves were obtained by pulling until complete detachment: (a) a spiral thread from a radial thread; (b) a spiral thread from a radial thread connected to another spiral thread; (c) a spiral thread from a complex system with more than one spiral thread connected to a single radial thread; (d) a radial thread from a radial thread. Images reveal that junctions involving either spiral and radial threads or only radial threads are characterized by different morphology. Scale bar: 10 μm .

case (Fig. S3). The NSR sample (type c) showed an average force at break of 1.3 ± 0.5 mN, dissipated energy of 7.4 ± 5.5 μJ with the corresponding mean displacement at break being 19 ± 5 mm (Fig. 4). After the rupture of the junction linked to the spiral thread where the force was applied, the remaining structure resulted undamaged (Fig. S4). The mean maximum load that the TRR junction (type d) can withstand was 9 ± 2 mN, its dissipated energy was 19 ± 8 μJ with a corresponding displacement at break of 5 ± 1 mm (Fig. 4). The supporting radial thread resulted undamaged after the junction failure (Fig. S5). Finally, the anchorage sample showed an average







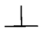

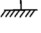
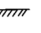
Type of junction	Failure mode	Force at break	Displacement at break	Energy dissipated at break
a) Spiral from Radial (TSR) 		0.4 ± 0.2 mN	9 ± 4 mm	1.5 ± 1.1 μ J
b) Spiral from Radial (CSR) 		0.9 ± 0.2 mN	10 ± 5 mm	3.4 ± 1.8 μ J
c) Spiral from Radial (NSR) 		1.3 ± 0.5 mN	19 ± 5 mm	7.4 ± 5.5 μ J
d) Radial from Radial (TRR) 		9 ± 2 mN	5 ± 1 mm	19 ± 8 μ J
e) Radial from a surface (RFS) 		18 ± 10 mN	2.9 ± 1.2 mm	26 ± 10 μ J

Figure 4. Maximum load/displacement and toughness obtained after testing different web samples. All displacements are referred to an initial length of 0.5 cm. The second column reports what is left after the sample failure: in all the tested configurations, the supporting structure resulted unbroken after the junction failure (i.e., complete detachment of the pulled thread). The toughness was computed by calculating the area under the load-displacement curves.

force at break of 18 ± 10 mN, dissipated energy of 26 ± 10 μ J, with the corresponding mean displacement at break being 2.9 ± 1.2 mm (Fig. 4). The initial length of the pulled thread was 0.5 cm in all the tested specimens.

In order to interpret the differences among the force values recorded for each junction sample, we performed both ANOVA and Weibull Statistics analysis (Tables S1–S5, S9 and Supporting Figs S6–S11). In particular, junction separation forces differed significantly across all junction types (ANOVA, $p \sim 0$, all post-hoc pairwise comparisons $p < 0.05$). Interestingly, the highest p -value (~ 0.02) was observed for CSR and NSR junctions (Table S9). Indeed, the Weibull distributions obtained from the data available for CSR and NSR samples are very similar, while the distributions corresponding to the samples that involve radial threads show a much larger difference with respect to those that involve spiral threads.

Discussion

Two features common to all the tested samples are concerned with the maximum force, which is recorded when the pulled thread detaches completely from its junction (Figs S2–S5 and Videos S1–S5), and the shape of the sample after the mechanical test, whose structure (consisting of either another thread or a more complex architecture) looks the same as before the test, except for the pulled thread. This indicates the ability of the web structure to localize the damage regardless the size of its analyzed portion.

Regarding the structural properties collected in Figs 3 and 4, we can immediately see that junctions involving only radial threads, such as TRR or RFS configurations, which are mainly composed of pyriform silk, are much stronger (23 times and 46, respectively, compared to TSR) yet tougher (with a dissipated energy of 13 and 26 times bigger than that of TSR sample, respectively) than those involving spiral threads, which are mainly composed of aggregate silk. Such result is also supported by the statistical analysis of the breaking force (Tables S1–S5, S8 and Figs S6–S11). This can be easily explained by recalling the different position that such junctions occupy within the web structure. In particular, junctions between radial threads, which are located at the edge of the web, must support higher loads (e.g. high-speed wind) in comparison to the region embedded within the boundary of the web that has mainly the function to stop preys. In this region, aggregate silk joins the spiral threads to radial threads, providing the spider's web with its classical orb shape. Spiral-radial thread junctions act as filters for choosing the appropriate prey for the spider and for avoiding useless damage of the cobweb. As big loads could be fatal to the structure, causing an extended and irreversible damage, high kinetic energy objects are allowed to pass through the web by producing a localized rupture, e.g. of a single junction (that thus behaves as a sacrificial element). The existence of two different types of junction becomes thus necessary, with one (i.e., pyriform based junction) for sustaining high loads and holding the structure as a whole and the other one (i.e., aggregate based junction) for catching preys without compromising the integrity of the entire structure and allowing spiders to save energy in rebuilding the web after an impact¹⁷. Finally, it can be observed from our tests that when we pull a radial thread out of a spiral-radial thread junction, the stiffness of the supporting structure plays a role in determining the mechanical properties of the web sample. Indeed, moving from TSR to CSR and NSR, the increase of structural complexity and stiffness, given by the addition of one or more spiral threads connected to the same radial thread, leads to an increase of the maximum force, and also an increase of displacement at break and dissipated energy (Tables S6–S8). This agrees also to what found for configuration TRR, that is stiffer and tougher than TSR sample. Radial threads are themselves stiffer than spiral ones, with a Young modulus of ~ 1 GPa, that is one order of magnitude bigger than that of spiral threads (~ 0.1 GPa). By referring to the force increase in CSR (2.4) and NSR (3.3) with respect to TSR samples (Table S5), this tends to saturate with the increase of complexity (e.g., stiffness) of the structure itself (the force at break of NSR is only 1.4 bigger than that for CSR in spite of the addition of a number of threads). This suggests that after a certain number of threads added to the anchor, there is no more increase in the junction load bearing capacity.

Conclusion

A 400 million years evolution has designed the orb web as a structure simultaneously able to stop flying prey, localize damage after impacts and withstand high loads. The interaction among the threads and their anchorages to the substrate could provide an explanation to the mechanical efficiency of the orb webs. This interaction is mediated by the presence of junctions that connect threads to each other or to the surrounding environment. In this work, we observed that two different types of junction exist and we measured the force necessary to break them in different configurations. The first type seems to be made of aggregate silk that is used by spiders for joining radial and spiral threads as well as to provide spiral threads with sticky droplets. The second type seems to be composed of pyriform silk that is mainly used for joining either radial threads together and/or radial threads with the substrate. The first type of junction showed a lower breaking force with respect to the second type, even if an increase in both the force and displacement at break was observed as associated to an increased structural complexity. This difference in terms of breaking force can be explained by considering the different roles that these kinds of junction play in the orb web. Indeed, junctions between two radial threads and between radial threads and surfaces have to withstand higher loads since these support the whole web structure, while junctions involving spiral threads have to guarantee damage localization (e.g., web robustness), thus breaking at lower loads.

Our work could provide new information that shed light on the mechanical behavior of spider's orb web and could be used for the design of new bio-inspired nets and fabrics with superior mechanical properties.

Methods

Spiders care and web production. The spider under study was *Nuctenea umbratica* (Clerck 1876), common nocturnal spider that usually builds its web during the night. We kept three individuals in glass terrarium of about $30 \times 30 \times 40$ cm. All spiders were adult females and fed with a weekly diet of *Blaptica dubia* that were breed in the “Laboratory of Bio-inspired and Graphene Nanomechanics” and fed weekly with carrots and fish food. All terrariums were set in the same way with three long sticks covered with paper attached to the wall of the terrarium. Each terrarium was provided with a small refuge, made of paper, in the right corner of the cage to allow the spider to feel protect and live without stress during the day. Each spider produced its orb web after a few days.

Sample preparation. The tested samples were prepared by following the same procedure reported by Blackledge *et al.*³⁰ and Grawe *et al.*²⁴ We stuck the web samples on a paper frame provided with a square window of 1 cm side. The web sample was fixed to the paper frame with a double-sided tape. We checked the direction of the spinning process before collecting web samples. By referring to the anchorages, we stuck black paper on the terrarium walls where the spider spins the attachment disc. Then we cut the portion of the paper containing the anchorage and fix it on a wood block ($2 \times 0.5 \times 0.5$ cm³). This block was fixed to the previous paper support by attaching the radial thread to the upper part of the frame.

Optical and SEM images. For the morphology characterization, we used an Optical microscope (Jenavert) with a 20x enlargement lens. The microscope was provided with a camera (Canon) connected to a computer for remote control.

For the SEM characterization, we used a Zeiss – 40 Supra. The metallization was made by using a sputtering machine Q150T and the sputtering mode was Pt/Pd 80:20 for 5 minutes. For the Fig. 1b we did not metalize the sample and the picture was taken at 2.0 kV, 1300 Magnification with secondary electron detector. For the Fig. 1c the picture was taken at 2.0 kV, 103 Magnification and with secondary electron detector. With reference to Fig. 2b–e the pictures were taken at 2.0 kV, 15 kV, 2.0 kV and 15.0 kV, 1290, 5580, 2520 and 641 magnifications, respectively, with the secondary electron detector in all cases.

Mechanical characterization. For the mechanical characterization, we used a nanotensile testing machine (Agilent technologies T150 UTM) with a load cell of 500 mN. The displacement speed was $10 \mu\text{m}$ per second with the frequency load at 20 Hz. The samples were mounted in order to pull a spiral or radial thread out (depending on the sample) in the direction opposite to spider spinning. The declared sensitivity of the machine is 10 nN for the load and 1 Å for the displacement in the dynamic configuration. The tests were recorded with a Sony Camera. Ten samples were tested for each configuration.

Data Availability

The authors declare that the data supporting the findings of this study are available within the article and its supplementary information files.

References

1. Foelix, R. *Biology of Spider*. Oxford University Press 53 (2011).
2. Nentwig, W. *Spider ecophysiology*. *Spider Ecophysiology*, <https://doi.org/10.1007/978-3-642-33989-9> (2013).
3. Madsen, B., Shao, Z. Z. & Vollrath, F. Variability in the mechanical properties of spider silks on three levels: Interspecific, intraspecific and intraindividual. *Int. J. Biol. Macromol.* **24**, 301–306 (1999).
4. Plaza, G. R., Guinea, G. V., Pérez-Rigueiro, J. & Elices, M. Thermo-hygro-mechanical behavior of spider dragline silk: Glassy and rubbery states. *J. Polym. Sci. Part B Polym. Phys.* **44**, 994–999 (2006).
5. Das, R. *et al.* Biomechanical characterization of spider webs. *J. Mech. Behav. Biomed. Mater.* **67**, 101–109 (2017).
6. Plaza, G. R. *et al.* Relationship between microstructure and mechanical properties in spider silk fibers: identification of two regimes in the microstructural changes. *Soft Matter* **8**, 6015 (2012).
7. Guinea, G. V., Elices, M., Pérez-Rigueiro, J. & Plaza, G. Self-tightening of spider silk fibers induced by moisture. *Polymer (Guildf)*. **44**, 5785–5788 (2003).
8. Perez-Rigueiro, J. The effect of spinning forces on spider silk properties. *J. Exp. Biol.* **208**, 2633–2639 (2005).
9. Vollrath, F. Biology of spider silk. *Int. J. Biol. Macromol.* **24**, 81–88 (1999).
10. Cetinkaya, M., Xiao, S., Markert, B., Stacklies, W. & Gräter, F. Silk fiber mechanics from multiscale force distribution analysis. *Biophys. J.* **100**, 1298–1305 (2011).

11. Kluge, J. A., Rabotyagova, O., Leisk, G. G. & Kaplan, D. L. Spider silks and their applications. *Trends Biotechnol.* **26**, 244–251 (2008).
12. Vollrath, F. & Porter, D. Spider silk as archetypal protein elastomer. *Soft Matter* **2**, 377 (2006).
13. Lewis, R. V. Spider Silk: Ancient Ideas for New Biomaterials Spider Silk: Ancient Ideas for New. *Biomaterials.* **106**, 3762–3774 (2006).
14. Eisoldt, L., Smith, A. & Scheibel, T. Decoding the secrets of spider silk. *Mater. Today* **14**, 80–86 (2011).
15. Boutry, C. & Blackledge, T. A. Wet webs work better: humidity, supercontraction and the performance of spider orb webs. *J. Exp. Biol.* **216**, 3606–3610 (2013).
16. Asakura, T. & Miller, T. *Biotechnology of Silk.* **5** (2014).
17. Cranford, S. W., Tarakanova, A., Pugno, N. M. & Buehler, M. J. Nonlinear material behaviour of spider silk yields robust webs. *Nature* **482**, 72–76 (2012).
18. Pugno, N. M., Cranford, S. W. & Buehler, M. J. Synergetic material and structure optimization yields robust spider web anchorages. *Small* **9**, 2747–2756 (2013).
19. Blasingame, E. *et al.* Pyriform spidroin 1, a novel member of the silk gene family that anchors dragline silk fibers in attachment discs of the black widow spider, *Latrodectus hesperus*. *J. Biol. Chem.* **284**, 29097–29108 (2009).
20. Kooor, J. & Zylberberg, L. Fine structural aspects of silk secretion dladematus. In the. *Tissue Cell* **12**, 547–556 (1980).
21. Kooor, J. & Zylberberg, L. Fine structural aspects of silk secretion in a spider. *Tissue Cell* **14**, 519–530 (1982).
22. Pugno, N. M. The theory of multiple peeling. *Int. J. Fract.* **171**, 185–193 (2011).
23. Brely, L., Bosia, F. & Pugno, N. M. Numerical implementation of multiple peeling theory and its application to spider web anchorages. *Interface Focus* **5**, 20140051 (2015).
24. Grawe, I., Wolff, J. O. & Gorb, S. N. Composition and substrate-dependent strength of the silken attachment discs in spiders. *J. R. Soc. Interface* **11**, 20140477–20140477 (2014).
25. Wolff, J. O., Van der Meijden, A. & Herberstein, M. E. Distinct spinning patterns gain differentiated loading tolerance of silk thread anchorages in spiders with different ecology. *Proc. R. Soc. B Biol. Sci.* In Press (2017).
26. Wolff, J. O., Grawe, I., Wirth, M., Karstedt, A. & Gorb, S. N. Spider's super-glue: thread anchors are composite adhesives with synergistic hierarchical organization. *Soft Matter* **11**, 2394–2403 (2015).
27. Meyer, A., Pugno, N. M. & Cranford, S. W. Compliant threads maximize spider silk connection strength and toughness. *J. R. Soc. Interface* **11**, 20140561–20140561 (2014).
28. Vasanthavada, K. *et al.* Spider glue proteins have distinct architectures compared with traditional spidroin family members. *J. Biol. Chem.* **287**, 35985–35999 (2012).
29. Opell, B. D. & Schwend, H. S. Adhesive efficiency of spider prey capture threads. *Zoology* **112**, 16–26 (2009).
30. Blackledge, T. A. Quasistatic and continuous dynamic characterization of the mechanical properties of silk from the cobweb of the black widow spider *Latrodectus hesperus*. *J. Exp. Biol.* **208**, 1937–1949 (2005).

Acknowledgements

The authors would like to thank Lorenzo Moschini, Prof. Antonella Motta and Prof. Claudio Migliaresi (Biotech – Mattarello, University of Trento) for their support with SEM images. N.M.P. is supported by the European Commission under the Graphene Flagship Core 2 grant No. 785219 (WP14 “Composites”) and FET Proactive “Neurofibres” grant No. 732344 as well as by the Italian Ministry of Education, University and Research (MIUR) under the “Departments of Excellence” grant L.232/2016 and ARS01-01384-PROSCAN.

Author Contributions

N.M.P. supervised the study and the data analyses. G.G. and M.F.P. designed the study, performed the experiments, acquired the data and wrote the manuscript. B.M. and N.M.P. helped to write the manuscript. All authors viewed and approved the final manuscript and had the opportunity to comment on earlier drafts.

Additional Information

Supplementary information accompanies this paper at <https://doi.org/10.1038/s41598-019-42070-8>.

Competing Interests: The authors declare no competing interests.

Publisher's note: Springer Nature remains neutral with regard to jurisdictional claims in published maps and institutional affiliations.



Open Access This article is licensed under a Creative Commons Attribution 4.0 International License, which permits use, sharing, adaptation, distribution and reproduction in any medium or format, as long as you give appropriate credit to the original author(s) and the source, provide a link to the Creative Commons license, and indicate if changes were made. The images or other third party material in this article are included in the article's Creative Commons license, unless indicated otherwise in a credit line to the material. If material is not included in the article's Creative Commons license and your intended use is not permitted by statutory regulation or exceeds the permitted use, you will need to obtain permission directly from the copyright holder. To view a copy of this license, visit <http://creativecommons.org/licenses/by/4.0/>.

© The Author(s) 2019

1 **Supplementary information**

2 **Imaging and mechanical characterization of different junctions in spider**
3 **orb webs**

4 Gabriele Greco ^{1,2}; Maria F. Pantano ¹; Barbara Mazzolai² and Nicola Pugno ^{1,3,4*}

5 ¹ Laboratory of Bio-Inspired & Graphene Nanomechanics, Department of Civil, Environmental and
6 Mechanical Engineering, University of Trento, Via Mesiano, 77, 38123 Trento, Italy

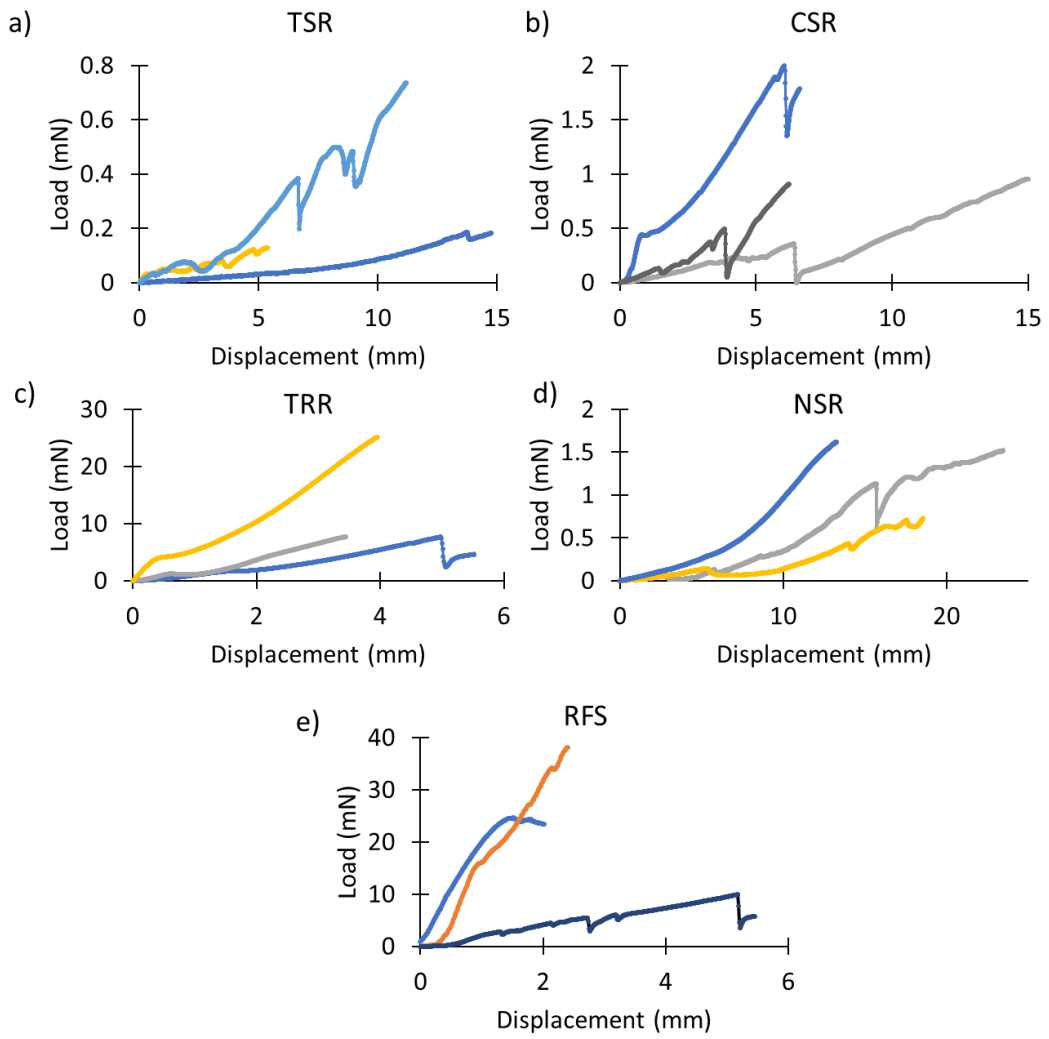
7 ² Center for Micro-BioRobotics@SSSA, Istituto Italiano di Tecnologia, Viale Rinaldo Piaggio 34, I-
8 56025 Pontedera, Italy

9 ³School of Engineering and Materials Science, Queen Mary University of London, Mile End Road, E1
10 4NS London, United Kingdom

11 ⁴Ket-Lab, Edoardo Amaldi Foundation, Via del Politecnico snc, 00133 Rome, Italy

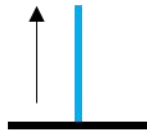
12 *Corresponding author: nicola.pugno@unitn.it

13

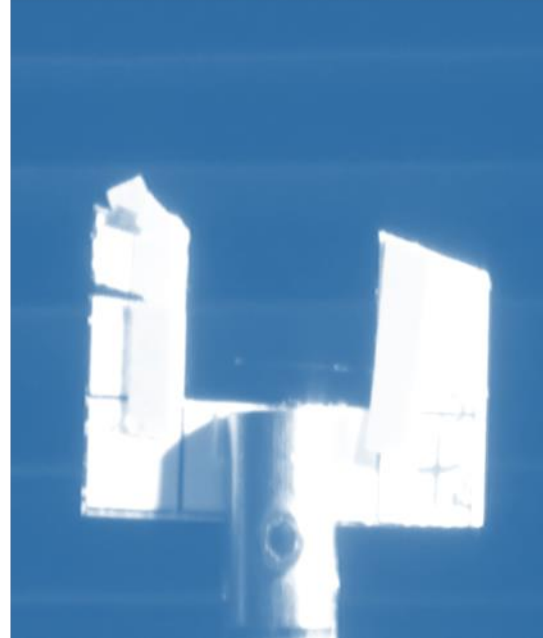
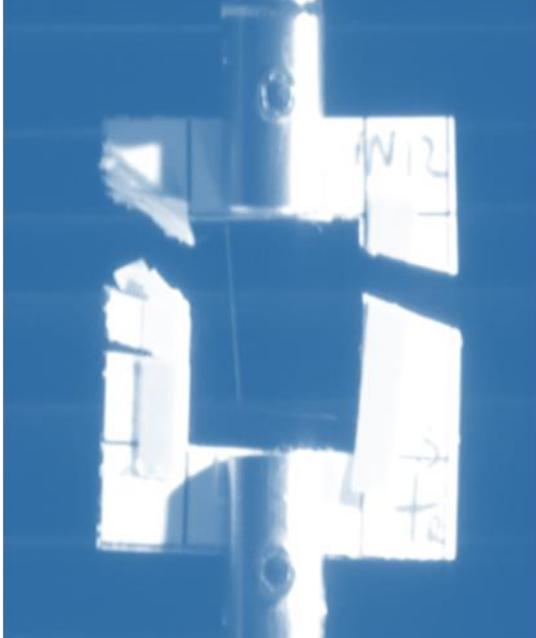


16 *Figure S1: Three representative load-displacement curves observed for a) TSR, b) CSR, c) TRR, d) NSR, e) RFS samples.*

a)



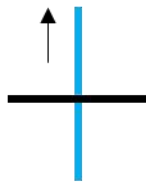
b)



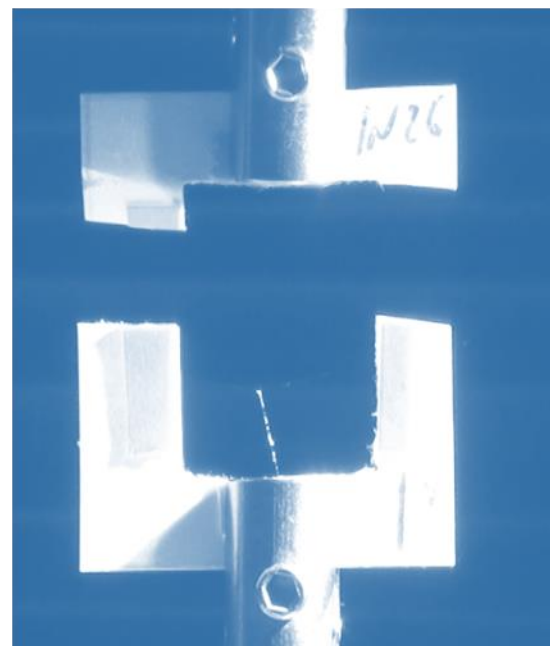
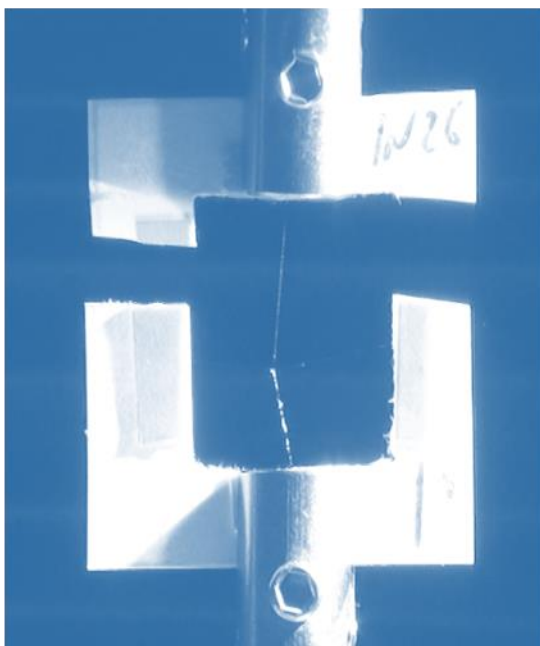
17

18 *Figure S2: A TSR sample before (a) and after the test (b).*

a)

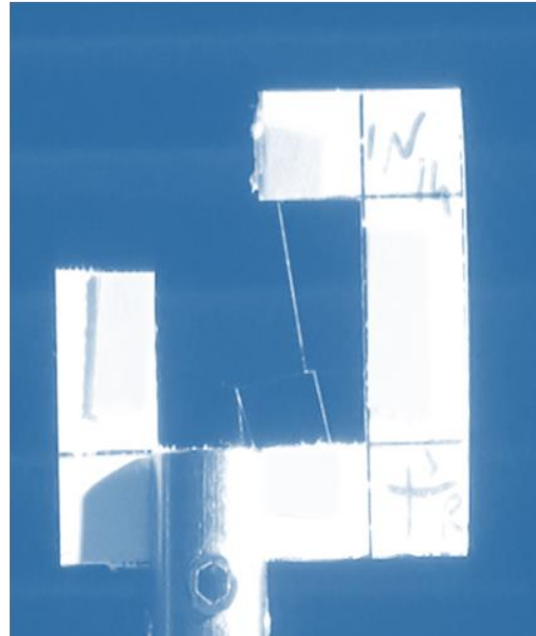
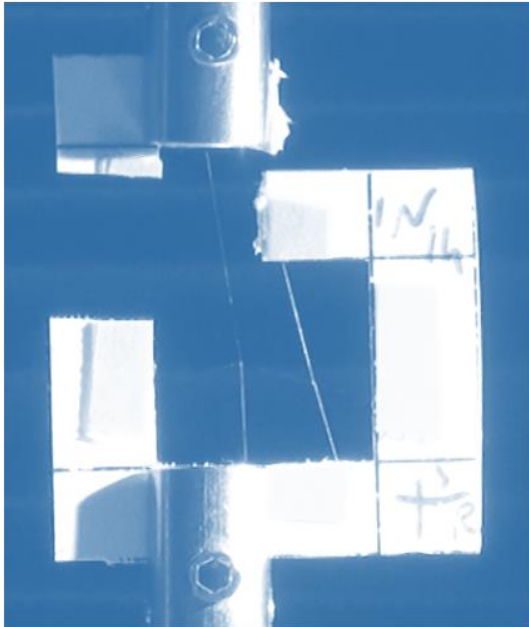
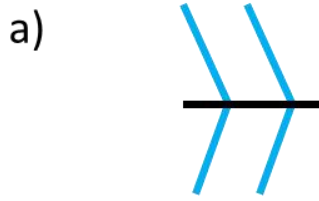


b)



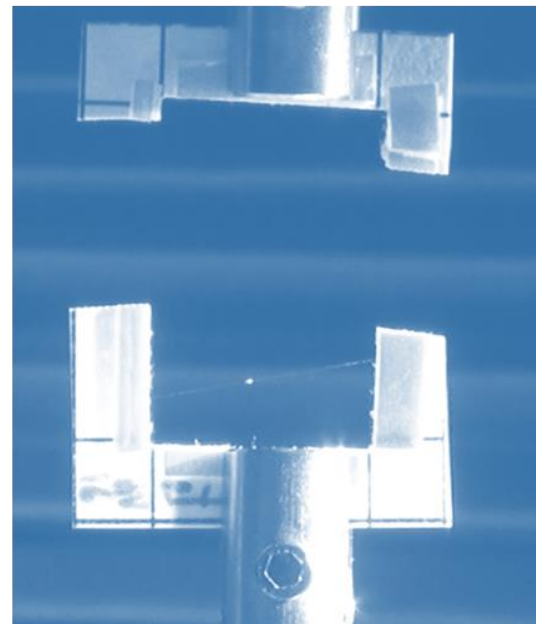
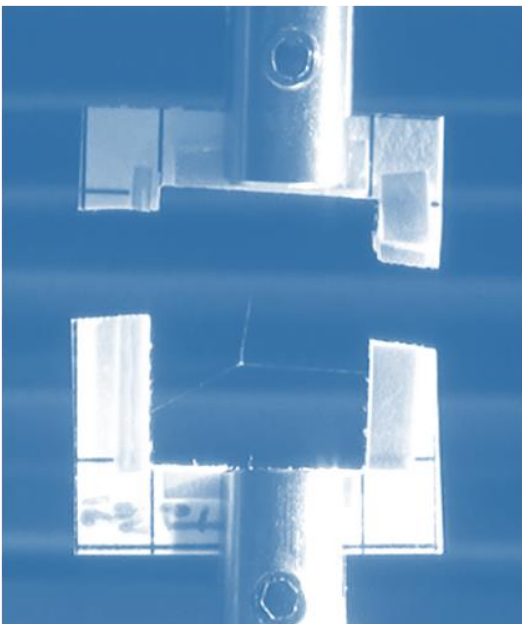
19

20 *Figure S3: A CSR sample before (a) and after (b) the test.*



21

22 *Figure S4: An NSR sample before (a) and after (b) the test.*



23

24 *Figure S5: A TRR sample before (a) and after (b) the test.*

Sample (TSR)	Force at break (mN)	Displacement at break (mm)	Energy dissipated at break (μ J)
1	0.74	8.99	3.26
2	0.13	10.26	0.15
3	0.56	4.15	1.20
4	0.43	11.26	1.00
5	0.33	14.90	1.86
6	0.51	11.19	1.12
7	0.42	5.37	1.90
8	0.37	7.11	1.03
9	0.18	7.00	0.36
10	0.31	13.75	3.14

25 *Table S.1.: Results from tests on TSR sample.*

26

27

28

29

30

31

32

33

34

35

Sample (CSR)	Force at break (mN)	Displacement at break (mm)	Energy dissipated at break (μ J)
1	0.91	10.26	2.00
2	1.13	5.85	2.93
3	1.13	6.20	6.42
4	0.92	5.74	3.03
5	0.90	17.36	2.95
6	0.71	14.13	2.24
7	0.66	11.97	5.80
8	0.62	8.05	1.52
9	0.98	15.40	4.29
10	1.01	2.97	1.12

36 *Table S.2.: Results from tests on CSR sample.*

37

38

39

40

41

42

43

44

45

46

Sample (NSR)	Force at break (mN)	Displacement at break (mm)	Energy dissipated at break (μ)
1	1.72	15.15	4.02
2	1.59	20.00	10.29
3	0.65	21.02	16.62
4	1.26	22.71	7.10
5	1.11	10.86	3.98
6	0.85	24.75	5.19
7	1.66	20.97	4.16
8	0.73	18.56	13.74
9	1.65	14.27	4.04
10	1.36	24.78	4.45

47

48 *Table S.3.: Results from tests on NSR sample.*

49

50

51

52

53

54

55

56

57

Sample (TRR)	Force at break (mN)	Displacement at break (mm)	Energy dissipated at break (μ J)
1	7.35	5.12	14.26
2	7.70	4.85	7.16
3	12.87	3.22	29.78
4	7.55	5.55	21.65
5	7.70	4.91	19.06
6	10.00	5.00	12.57
7	9.85	3.44	25.17
8	10.16	5.00	28.56
9	9.44	4.98	17.65
10	11.80	6.59	12.40

58 *Table S.4: Results from tests TRR sample.*

59

60

61

62

63

64

65

66

67

68

Sample (RFS)	Force at break (mN)	Displacement at break (mm)	Energy dissipated at break (μ J)
1	10.01	1.90	36.19
2	24.70	1.56	10.96
3	15.57	2.32	33.20
4	31.15	3.04	34.73
5	38.13	4.20	43.45
6	15.05	3.03	25.89
7	14.40	1.78	16.29
8	9.30	2.26	14.43
9	15.96	3.33	24.03
10	9.91	5.17	26.25

69 *Table S.5: Results from tests on RFS sample.*

70

Compared samples	Ratio between dissipated energies
TRR/TSR	13
RFS/TRR	2.0
CSR/TSR	2.3
NSR/TSR	4.9
NSR/CSR	2.2

71 *Table S.6: Comparison between the energy required to break different samples.*

Compared samples	Ratio between detachment forces
TRR/TSR	23
RFS/TRR	2.0
CSR/TSR	2.4
NSR/TSR	3.3
NSR/CSR	1.4

72 *Table S.7: Comparison between the detachment forces of different samples.*

73

Compared samples	Ratio between displacement at break
TRR/TSR	0.56
RFS/TRR	0.58
CSR/TSR	1.9
NSR/TSR	2.1
NSR/CSR	1.4

74 *Table S.8: Comparison between the displacements at break of different samples.*

75

76 **Statistical analysis**

77 ANOVA Analysis

78 Analysis of variance was performed to compare the mean values of the forces at break.

79 The parameters used to verify the null hypothesis, i.e. all the data sets come from the same

80 distribution and have the same mean value, were

81
$$SSQ_a = \sum_{g=1}^G n_g (m_g - m)^2$$

82

$$SSQ_e = \sum_{g=1}^G \sum_{j=1}^{n_g} (x_{gj} - m_g)^2$$

83

84

85

Where G is the number of different samples under consideration, n_g is the number of tests of the same sample, m is the mean value of all the data, m_g is the mean value within the group (i.e., sample), and x is the single force value. These sums of squares were used to compute the T value

86

$$T = \frac{\frac{SSQ_a}{G-1}}{\frac{SSQ_e}{n-G}}$$

87

88

89

90

91

92

that has been compared with the ideal value of the Fisher function F with a significance level of 5%. If $T > F$ we reject the null hypothesis and thus we can consider the difference among the data set as significant (i.e., the difference is due to intrinsic differences among the samples and not a consequence of internal variance). In our case, $g=10$, $G=5$ or 2 (according to the number of samples considered in the comparison), $n=50$ or 20 (according to the number of samples considered in the comparison). The p-value was computed with the support of MatLab®.

93

94

95

96

Table S9 shows that the difference among all the studied samples is significant. The relatively small difference in T value between CSR and NSR samples confirms the hypothesis that the magnitude of the force at break saturates with the increase in complexity (and thus stiffness) of the sample structure.

97

	ALL	TSR CSR	TSR NSR	TSR TRR	TSR RFS	CSR NSR	CSR TRR	CSR RFS	NSR TRR	NSR RFS	TRR RFS
SSQa	2459.30	5.72	3.70	408.97	1623.60	0.65	365.09	1534.93	1807.22	1472.33	402.84
SSQe	892.39	0.59	1.78	32.62	858.28	1.78	32.63	858.29	33.82	859.48	890.32
T	31.00	175.49	37.48	225.67	34.05	6.58	201.42	32.19	961.96	30.83	8.14
F	2.61	4.41	4.41	4.41	4.41	4.41	4.41	4.41	4.41	4.41	4.41
p-value	~0	~0	0.00000 952	~0	0.00001 596	0.0194 7250	~0	0.00002 293	~0	0.00003 345	0.0105617 8

98

99

100

Table S9: Values of the ANOVA analysis performed on the load at break of the different types of tested junctions. The first column reports the comparison among all the types of junction samples, while and the following columns report the comparison between two different samples (all combinations).

101

102

103

104

105 Weibull Statistics

106 Weibull statistics was also considered in order to evaluate the force at break distribution across our
107 different samples. The main Weibull parameters, namely scale and shape parameters, were derived
108 from a linear regression fit implemented in the Matlab® software environment.

109 We considered the cumulative density function, CF , defined as

110
$$CF(F, m, F_0) = 1 - e^{-\left(\frac{F}{F_0}\right)^m}$$

111 where F is the force at break of the sample, m is the shape parameter and F_0 the scale parameter.

112 For the linear regression fit, we used the median rank estimator

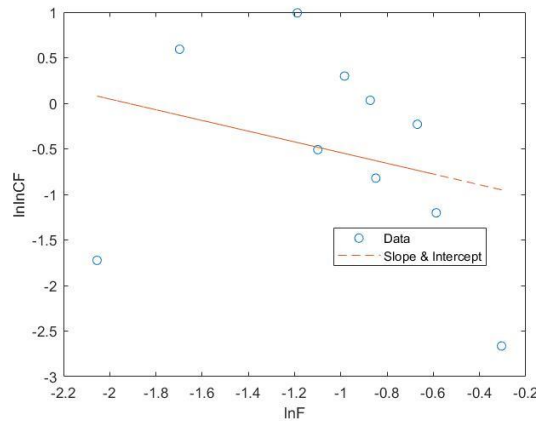
113
$$\widehat{CF}(F, M, F_0) = \frac{i - 0.3}{n + 0.4}$$

114 where i is the position of the sample with respect to the maximum among the data and n is the
115 number of tested samples. From the double logarithm

116
$$\ln\left(\ln\left(\frac{1}{1 - \widehat{CF}}\right)\right) = m \ln(F) - m \ln(F_0)$$

117 we can estimate the Weibull parameters m and F_0 (Figures S6-S10), which then allows to model the
118 probability density distribution corresponding to the force at break of all our samples (Figure S11).

119



120

121

Fig S6: Weibull linear regression method applied to the TSR sample.

122

123

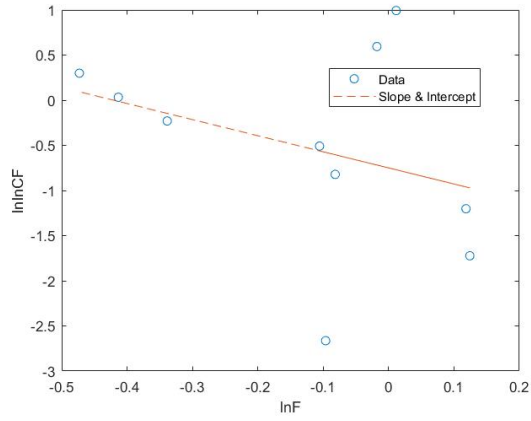


Fig S7: Weibull linear regression method applied to the CSR sample.

124

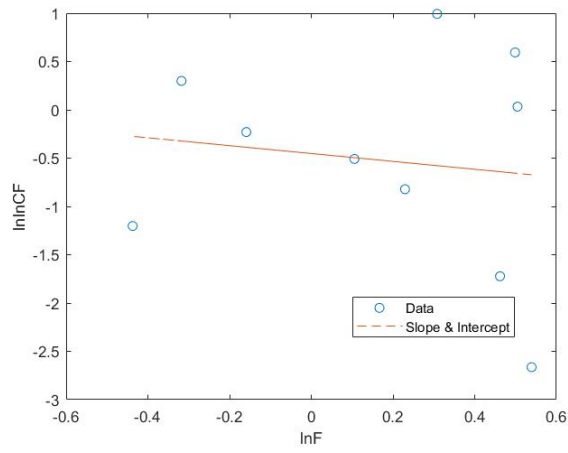


Fig S8: Weibull linear regression method applied to the NSR sample.

125

126

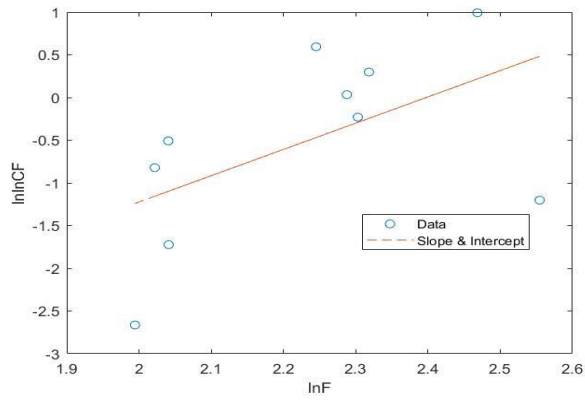


Fig S9: Weibull linear regression method applied to the TRR sample.

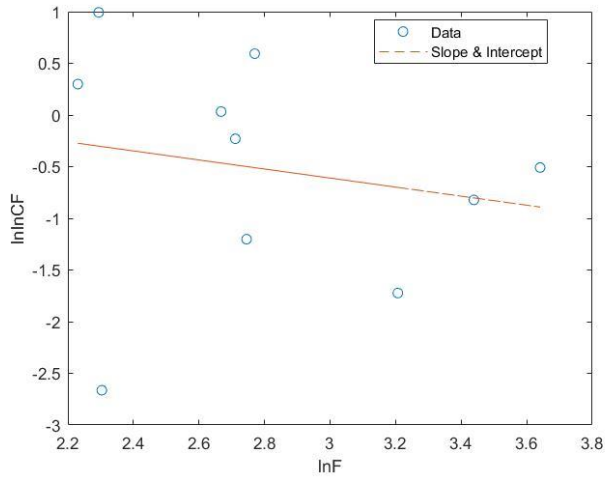


Fig S10: Weibull linear regression method applied to the RFS sample.

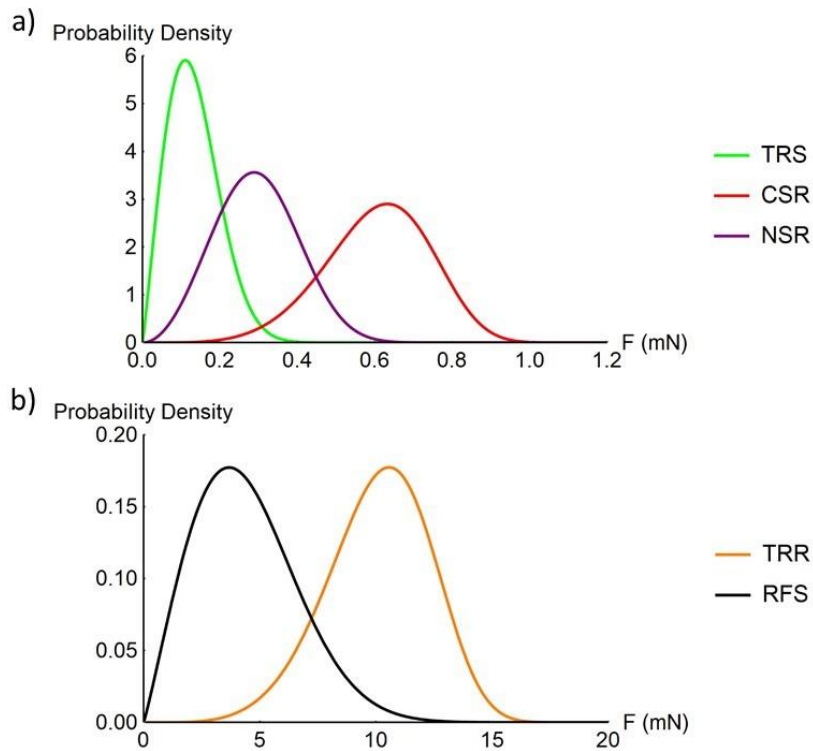


Fig S11: Weibull probability density function of the force required to break different web samples during a tensile test. a) TRS, CSR and NSR samples fail at forces significantly smaller than TRR and RFS samples (b). Note that in the first set of samples (a) a spiral thread is pulled out of the corresponding web sample during the test, while in the second set of samples (b) a radial thread is pulled out.